Where does subduction initiate and cease? A global scale perspective

Martina M Ulvrova, Nicolas Coltice, Simon Williams, Paul J Tackley

▶ **To cite this version:**

Martina M Ulvrova, Nicolas Coltice, Simon Williams, Paul J Tackley. Where does subduction initiate and cease? A global scale perspective. Earth and Planetary Science Letters, 2019, 528, pp.115836. 10.1016/j.epsl.2019.115836 . hal-03228622

HAL Id: hal-03228622
https://hal.science/hal-03228622

Submitted on 18 May 2021

HAL is a multi-disciplinary open access archive for the deposit and dissemination of scientific research documents, whether they are published or not. The documents may come from teaching and research institutions in France or abroad, or from public or private research centers.

L'archive ouverte pluridisciplinaire **HAL**, est destinée au dépôt et à la diffusion de documents scientifiques de niveau recherche, publiés ou non, émanant des établissements d'enseignement et de recherche français ou étrangers, des laboratoires publics ou privés.

Where does subduction initiate and cease? A global scale perspective.

Martina M. Ulvrova[1], Nicolas Coltice[2], Simon Williams[3], and Paul J. Tackley[1]

Corresponding author: M. Ulvrova, Department of Earth Sciences, Institute of Geophysics, ETH Zürich, Sonneggstrasse 5, Zürich, 8092, Switzerland. (martina.ulvrova@erdw.ethz.ch)

[1]Institute of Geophysics, Department of Earth Sciences, ETH Zürich, Zürich, Switzerland.

[2]Laboratoire de Géologie, École Normale Supérieure, CNRS-UMR 8538, PSL Research University, Paris, France

[3]EarthByte Group, School of Geosciences, University of Sydney, Sydney, New South Wales, Australia

Abstract. The thermo-mechanical evolution of the Earth's mantle is largely controlled by the dynamics of subduction zones, which connect the surface tectonic plates with the interior. However, little is known about the systematics of where subduction starts and stops within the framework of global plate motions and evolving continental configurations. Here, we investigate where new subduction zones preferentially form, and where they endure and cease using statistical analysis of large-scale simulations of mantle convection that feature self-consistent plate–like lithospheric behaviour and continental drift in the spherical annulus geometry. We juxtapose the results of numerical modelling with subduction histories retrieved from plate tectonic reconstruction models and from seismic tomography. Numerical models show that subduction initiation is largely controlled by the strength of the lithosphere and by the length of continental margins (for 2D models, the number of continental margins). Strong lithosphere favors subduction inception in the vicinity of the continents while for weak lithosphere the distribution of subduction initiation follows a random process distribution. Reconstructions suggest that subduction initiation and cessation on Earth is also not randomly distributed within the oceans, and more subduction zones cease in the vicinity of continental margins compared to subduction initiation. Our model results also suggest that intra-oceanic subduction initiation is more prevalent during times of supercontinent assembly (e.g. Pangea) compared to more recent continental dispersal, consistent with recent interpretations of relict slabs in seismic tomography.

1. Introduction

Subduction of the rigid plates is a fundamental process in Earth evolution, allowing chemical cycling between the surface and the deep mantle [Kerrick, 2001]. Indeed, the surface and interior of the planet are interconnected within a self-organized system in which subduction arises from an instability of the top boundary layer, while it also induces convective currents and pulls tectonic plates [Lowman, 2011; Coltice et al., 2017]. The evolution of the lithospheric plates including continents is then characterized by repeating Wilson cycles during which ocean basins periodically close and open while supercontinents assemble and disperse. However, little is known about subduction inception in the setting of global tectonics with floating continental rafts. How far from the continents do new subduction zones preferentially form? How do plate motions influence subduction inception? At which locations with respect to the position of the continental margins do subduction zones cease?

Few examples of active subduction inception or cessation are available to study. Young subduction systems can be found at the Mussau Trench [Hegarty et al., 1982] and Yap Trench [Lee, 2004] in the western Pacific, but it is not clear if these will develop into self-sustained subduction. Much of our knowledge on how subduction starts and stops is based on the geological record, including marine studies of forearcs [Reagan et al., 2010] and on-land studies of ophiolites [Dilek and Furnes, 2009], and on numerical modelling [e.g. Nikolaeva et al., 2010]. These studies indicate that subduction may initiate in a diverse range of tectonic settings; at passive margins [Nikolaeva et al., 2010], fracture zones such as for example Aleutian subduction zone [Maffione et al., 2017], at extinct spreading centres

such as for example Puysegur [Lebrun et al., 2003], adjacent to fossil island arcs [Leng and Gurnis, 2015], triggered by plumes [Gerya et al., 2015], or where mantle suction flow occurs [Baes et al., 2018]. Stern [2004] proposes two distinct mechanisms for subduction initiation: spontaneous nucleation by e.g. foundering at passive margins, or induced initiation involving forced convergence of existing plates.

In common with subduction initiation, cessation of subduction has been attributed to a variety of mechanisms, including collision with continents or oceanic plateaus, interaction between the subduction zone and spreading ridges and transforms, or within the context of a broader-scale reorganisation of plate motions [e.g. Michaud et al., 2006]. Some active subduction systems undergo a so-called polarity reversal, when the overriding plate becomes the subducting plate and vice versa. In such a case, subduction initiation and termination are directly related. An example of reversal of an active convergent boundary is the New Hebrides with the reversal of subduction of the Pacific beneath the Australian plate at the Vitiaz trench [Auzende et al., 1988].

A limiting factor in our current knowledge on subduction is the reliance on geological evidence collected on land, for example where former intra-oceanic subduction products have been accreted onto continents. Consequently, it is difficult to constrain where and when intra-oceanic arcs resided throughout their life cycle, and tectonic reconstructions are often dominated by subduction systems close to continents [e.g. Müller and Landgrebe, 2012]. Recently, studies mapping slab remnants imaged in seismic tomography [van der Meer et al., 2012; Domeier et al., 2017] point to the existence of previously unrecognized intra-oceanic subduction zones within the Pacific/Panthalassa domain that would have been active while Pangea was assembled or earlier in its dispersal, and much further from

the continents than more recent examples. This raises the question of how important the presence of continents is to the life cycle of subduction systems, and whether this influence varies between periods of supercontinent assembly and continental dispersal.

In this paper, we investigate the pattern of subduction initiation and cessation in time and space using numerical simulations of mantle convection. Numerical models are designed in a spherical annulus geometry, and we vary the number of continents, the strength of the lithosphere and its structure. We compare aspects of the modelling results to reconstructed subduction histories based on both plate kinematics and analysis of slab remnants imaged by seismic tomography [van der Meer et al., 2010, 2012; Müller et al., 2016]. We focus on global scale models to infer how the continental configuration and the plate layout change the distribution of subduction initiation and cessation, and the lifespan of subduction zones. The models indicate that subduction initiation is non-randomly distributed in the ocean, and cessation happens mostly in the vicinity of continents. Our calculations point to different distributions of subduction inception between phases of supercontinents and phases in which continents are dispersed..

2. Method

In order to investigate statistically the spatial relationships between continents and the initiation, evolution and cessation of subduction zones, we numerically calculate the solution of mantle convection in a spherical annulus [Hernlund and Tackley, 2008] using the StagYY code [Tackley, 2008]. The choice of geometry is motivated by the necessity of having long temporal series of several billions of years. Employment of the spherical annulus ensures similar scaling properties compared to the full 3D spherical shell. The model features self-consistently generated plate-like surface tectonics and drifting continents.

2.1. Physical and numerical model

We determine temperature, velocity, pressure and composition within the mantle by solving the equations of conservation of mass, momentum and energy and the advection of material composition considering an incompressible mantle under the Boussinesq approximation. Below, the equations are given in their dimensionless form.

$$\boldsymbol{\nabla} \cdot \boldsymbol{v} = 0\,, \tag{1}$$

$$\boldsymbol{\nabla} \cdot \left(\eta \left(\boldsymbol{\nabla} \boldsymbol{v} + (\boldsymbol{\nabla} \boldsymbol{v})^{\mathrm{T}}\right)\right) - \boldsymbol{\nabla} p = \mathrm{Ra}\,(T + B\,C)\,\boldsymbol{e}_{\mathbf{r}}\,, \tag{2}$$

$$\partial_t T + \boldsymbol{v} \cdot \boldsymbol{\nabla} T = \nabla^2 T + H\,, \tag{3}$$

$$\partial_t C + \boldsymbol{v} \cdot \boldsymbol{\nabla} C = 0\,, \tag{4}$$

with $\boldsymbol{v}$ the velocity, p the static pressure, η the viscosity, T the temperature, C the composition, H the internal heating rate, Ra the Rayleigh number, B the buoyancy ratio and $\boldsymbol{e}_{\mathrm{r}}$ the radial unit vector. ∂_t is the partial time derivative.

Viscosity η follows the Arrhenius law and is strongly temperature and pressure dependent

$$\eta(T, p) = \eta_A \exp\left(\frac{E_a + p\,V_a}{RT}\right)\,, \tag{5}$$

where $E_a = 166\,\mathrm{kJ\,mol^{-1}}$ is the activation energy (kept constant for all simulations), $V_{\mathrm{a}} = 6.34 \cdot 10^{-7}\,\mathrm{m^3\,mol^{-1}}$ the activation volume (constant for all simulations) and $R = 8.314\,\mathrm{J\,mol^{-1}\,K^{-1}}$ the gas constant. We give all parameters in Table 1. η_A is set such that η matches the reference viscosity η_0 at zero pressure and at temperature 1600 K, which is the expected temperature at the base of the lithosphere. We apply a viscosity cut off at 10^4 times η_0 . The viscosity varies over 6 orders of magnitude over the temperature variation ΔT, the superadiabatic temperature drop over the mantle. Independently of

temperature, viscosity increases exponentially by an order of magnitude with depth. The lowest values of the viscosity are in the asthenospheric mantle, while at the core mantle boundary viscosity is about 20 times lower than η_0.

To localize deformation in narrow zones and obtain realistic plate boundaries at the surface, we use a pseudoplastic rheology [Moresi and Solomatov, 1998; Tackley, 2000a, b]. After reaching a certain threshold value, the yield stress σ_{Y}, the rocks undergo plastic yielding. σ_{Y} is depth dependent and follows

$$\sigma_{\mathrm{Y}} = \sigma_0 + d\,\sigma'_{\mathrm{Y}}\,, \tag{6}$$

where σ_0 is the surface yield stress, d is the depth and σ'_{Y} is the yield stress depth derivative. If the stress reaches σ_{Y}, we calculate the effective viscosity η_{eff} on the grid

$$\eta_{\mathrm{eff}} = \min\left[\eta(T,p), \eta_{\mathrm{Y}}\right]\,, \tag{7}$$

with η_{Y} as

$$\eta_{\mathrm{Y}} = \frac{\sigma_Y}{2\dot{\epsilon}_{\mathrm{II}}}\,. \tag{8}$$

$\dot{\epsilon}_{\mathrm{II}}$ is the second invariant of the strain rate tensor. We vary the surface strength σ_0 of the lithosphere between 7 MPa and 56 MPa while keeping the gradient constant for all simulations at $810\,\mathrm{Pa\,m^{-1}}$.

Using this kind of rheology results in the self-consistent formation of strong plate interiors moving with a uniform velocity delimited by narrow plate boundaries characterized by reduced viscosity and an abrupt velocity change [Moresi and Solomatov, 1998; Tackley, 2000b]. Importantly, such rheology successfully reproduces seafloor age distributions [Coltice et al., 2012] and is sufficiently realistic to investigate global surface tectonics [Coltice et al., 2017; Ulvrova et al., 2019].

One of the important Earth-like features that is in general lacking in such convection models is single-sided subduction, i.e., subduction is often double-sided. This can be partially overcome by imposing a weak layer of oceanic oceanic crust at the surface, which gets advected into the subduction channel and hence decouples to a certain degree the sinking slab from the overriding plate, resulting in strong subduction asymmetry [Gerya et al., 2008; Crameri and Tackley, 2014]. In some of our simulations we include this weak crustal layer using tracers. The weak crustal layer is neutrally buoyant, and it follows the same viscosity law as ambient mantle but is characterized by a factor of 10 reduction in η_A and it is more easily deformable (surface yield stress 18 MPa, yield gradient $8.1\,\mathrm{Pa\,m^{-1}}$). The initial thickness of the weak crustal layer is 20 km and it is converted to a regular mantle after reaching 290 km depth. In one case, we further improve the model and obtain one-sided subduction zones by imposing a free surface that can vertically deform. This is done using the so-called sticky-air method [Matsumoto and Tomoda, 1983] when vertical deformation of the mantle surface is allowed by prescribing an additional layer of "air" atop of the mantle. This layer is permanently forced to be isothermal (300 K), has close to zero density and very low viscosity, allowing it to be decoupled from the lithosphere. To obtain a valid solution, the air layer must be sufficiently thick while having low viscosity [Crameri et al., 2012]. We fix its initial thickness to 150 km and keep its viscosity at 10^{-3} times η_0. This results in a high viscosity contrast between the plates at the surface and the air layer. The viscosity contrast is as high as 10^7.

Continental rafts are modeled using the tracer-ratio method [Tackley and King, 2003]. The detailed implementation is described elsewhere [Tackley and King, 2003; Rolf and Tackley, 2011]. We consider continents with an interior that is 300 km thick surrounded

by 140 km thick mobile belts in accordance with the thickness of the Archean cratons and Proterozoic belts. Continents cover 30% of the model surface. In order to ensure the stability of the continents, two conditions must be fulfilled: positive buoyancy and limited deformation within continents [e.g. Doin et al., 1997; Lenardic and Moresi, 1999]. Based on this, we choose a density contrast between continental material and ambient mantle of $-100\,\mathrm{kg\,m^{-3}}$, which gives the buoyancy ratio (ratio between the density contrast and the thermal density variation) of -0.4. Furthermore, continents are $100\times$ more viscous than the ambient mantle and do not undergo pseudo-plastic deformation. Due to this high rigidity, continental erosion by mantle flow is negligible and the rafts are stable over billions of years.

The system is driven by heating from radioactive elements and from heat conducted from the core. We keep the internal heating rate H constant at $5.44 \times 10^{-12}\,\mathrm{W\,kg^{-1}}$ throughout the simulations. Core heat loss contributes around 20% to the total surface heat flow, falling into the 10%–40% estimate for the Earth [Jaupart et al., 2015]. Both the top and the bottom boundaries are isothermal and free-slip, except for the case with a free deformable mantle surface, for which the top boundary of the computational domain is no-slip above the air layer.

The convective vigour of the system is measured by the Rayleigh number Ra

$$\mathrm{Ra} = \frac{\rho_0 g \alpha \Delta T D^3}{\kappa \eta_0}\,, \tag{9}$$

where ρ_0 is the reference density, g the gravitational acceleration, α the thermal expansivity, ΔT is the superadiabatic temperature drop across the mantle with the thickness D, κ is the thermal diffusivity and η_0 is the reference viscosity. For all experiments, we keep $\mathrm{Ra} = 10^6$ (calculated with $\eta_0 = 6 \times 10^{22}\,\mathrm{Pa\,s}$). This is $10 - 100\times$ lower than the

Earth's Rayleigh number, but lies at the edge of the computational feasibility for the given rheology and the presence of sticky air.

We use a resolution of 128×1024 cells in the radial and horizontal directions, respectively, except for the case with the free surface when we use a grid with 256×2048 cells. Vertical grid refinement close to the top and bottom limits is employed resulting in 10 km and 15 km (5 km and 8 km for the case with the sticky air) thick cells at the surface and at the core-mantle boundary (cf. more details in the supplementary material). To track composition, we use 4×10^7 tracers. This means that on average there are around 300 tracers per cell except in simulations with a free surface, which have higher resolution. In this case, the number of tracers per cell is around 75.

First, we run a model until it reaches a statistically steady state, at which the heat budget is balanced and characteristic properties of the system such as mean temperature, mean velocity and average surface heat flux fluctuate around some constant values. In this initial stage, we do not advect tracers and hence the composition field remains the same throughout the initialization period, which means that continents do not move from their initial positions. Once statistically steady state is achieved, we use a random snapshot from the equilibrated evolution to start the calculation with continents that move freely. The choice of the particular snapshot from the statistically steady state does not have any influence on the statistics performed on the system. The model is run until a sufficient number of subduction initiations N is collected. The shortest analyzed period is 1 Gy with 27 subduction initiation events. The longest analyzed period is 7 Gy with 288 detected subduction initiations. The length of the simulation does not have any influence on the results as soon as N is large enough and statistically representative of the system. The

parameters of the calculations are listed in Table 1. We vary the strength of the oceanic lithosphere and number of continents, and we test how the presence of the weak crustal layer and presence of a free surface alter the results. In total, we run 13 models having different parameterizations.

2.2. Model analysis

To detect subduction inception and follow its evolution, we analyze the divergence of the surface velocity. As soon as a negative peak of the surface velocity divergence appears (the threshold of detection being minus one tenth of the surface rms velocity), a new subduction zone is formed. The motion of this peak is then tracked through time and we record the distance to the closest continental margin until the peak disappears. For each case we specifically register this distance at subduction inception and at cessation. These values are further analyzed by calculating a cumulative distribution of the distance to the closest continental margin specifically when subduction starts and ends. To construct these distributions we bin the range of all possible distances into 500 km wide intervals. We then count the cumulative number of detected distances falling into a specific bin. All subduction zones that initiate at a continental margin fall into the first bin. The long duration of each model allows us to collect up to several hundreds of subduction initiations, typically several tens of them.

To investigate systematic patterns within the distributions retrieved from the models, we use a Monte Carlo method and calculate the synthetic distribution for subduction zones initiating at random positions within oceans. At each model time we generate a set of randomly located points within the oceans, which together we take to have a spatial distribution equivalent to scenarios where subduction intitiation or cessation locations

is also randomly distributed. For models with one continent, the cumulative frequency of random point locations as a function of distance to the continent is a straight line since the distance between the two continental margins is constant through time and the probability that a subduction zone initiates at a certain location is uniform. For more than one continent, the distribution is typically curved. This allows us to show how the modelled subduction distributions deviate from the random one. However, it is necessary that a sufficiently large number of random subduction initiations is generated at each time level, in total at least several thousand. To estimate the variance of the random distribution, we calculate distributions of N subduction initiation events that happen at random times and random positions. N is the number of initiations detected in the particular model.

3. Results

The organization of the system dictates its dynamic evolution: sinking slabs drive plate motion while inducing the mantle flow that in turn is at the origin of the plate motion (Figure 1). Plate-like behaviour is developed self-consistently using the yielding rheology (cf. Section 2.2) with a surface velocity that is constant in plate interiors while changing abruptly over plate boundaries. Since the system is heated mainly by internal heat sources (and we keep the internal heating rate constant for all simulations), sinking slabs and surface plates that compose the upper boundary layer dominate over plumes created at the core-mantle boundary. In particular, around 20% of the total surface heat flux is due to heating the mantle from the core. . The core derived fraction of the total surface heat flux is very similar for all models, with differences smaller than 1%. When looking at the temperature structure of the system (Figure 1b,e,h), one can note

that there is a strong subadiabatic gradient (Figure 1c,f,i). This is partly because the system is internally heated but more importantly negative gradients arise due to pressure dependent viscosity [Christensen, 1985].

Subduction zones (and in this study we refer to subduction zones as convective downwelling currents in the numerical simulations) next to continental margins are one-sided while a distinctive asymmetry is observed for intra-oceanic subduction zones (cf. Figure 1 and animation S1 in the supporting material). The degree of asymmetry in the latter case changes through time and differs among models. The dip angle with which plates sink into the mantle is generally large (close to vertical, Figure 1a) but more realistic behaviour is observed (i.e. shallower dip angles) in models with the weak crustal layer that allows partial decoupling between the sinking and overriding plates (Figure 1d), or in models with a free surface (Figure 1g). However, these models are still far from producing Earth-like subduction zones in their entirety, with modeled sinking plates commonly experiencing phases of symmetrical subduction during their lifespans, for example at their inception or during polarity flips (Figure 2). Crameri and Tackley [2014] have observed polarity reversals for intra-oceanic subduction in models with a similar parameterization but in 3D. Our models also show polarity reversals at the continent-ocean boundary (Figure 2).

3.1. Influence of lithospheric strength

To investigate the impact of the lithospheric strength on subduction initiation we run several models with different yield stress σ_0, which we vary between 7 and 56 MPa. The plate size hence number of subduction zones is strongly influenced by how difficult it is for the lithosphere to localize deformation, which is directly related to the value of σ_0. Decreasing the surface yield stress results in weaker oceanic lithosphere and smaller

plates [Moresi and Solomatov, 1998; Tackley, 2000b; Coltice et al., 2017; Langemeyer et al., 2018]. For low yield stress ($\sigma_0 = 7\,\mathrm{MPa}$), a large population of subduction zones exists at a given instant, fluctuating around 7 and 8 (cf. histogram on Figure 3a). The distribution of subduction initiation within the oceans can be characterized as a random process distribution as it follows the distribution of subduction zones that are randomly initiated in within oceans (Figure 3a). There are small deviations of the distribution from the mean synthetic random distribution, which fall into the variance of the random distribution. This is due to finite number of subduction zones collected for this model ($N = 89$). The fact that these deviations are small indicates that the number of subduction zones collected is sufficient. The number of subduction zones that are formed in the vicinity of a continental margin (closer than 500 km) is small, around 5% (Figure 3a). A stiffer lithosphere ($\sigma_0 = 35\,\mathrm{MPa}$, Figure 3b) promotes subduction initiation proximal to continents, with around 30% of subduction zones being formed close to continental margins. Within this case, the influence of the continents on subduction initiation is strongest close to the continents, which is in accordance with previous studies that showed stress focusing at the continental margins [Rolf and Tackley, 2011]. Beyond a certain threshold distance from the continents the probability of subduction initiation is essentially random. For intermediate yield stress ($\sigma_0 = 35\,\mathrm{MPa}$) this distance is around 3000 km (Figure 3b). For very stiff lithosphere ($\sigma_0 = 56\,\mathrm{MPa}$), the distance within which continents influence the stress distribution becomes greater still, with no clear threshold between random and controlled behaviour (Figure 3c). The frequency of subduction initiation in the immediate proximity of continental margins is further increased and is close to 40% for strong oceans with few (around two) subduction zones on average (Figure 3c and Figure 4a).

Subduction zones that are formed next to a continental margin stay glued to the continent their whole existence (Figure 5). In contrast, subduction zones that initiate as intra-oceanic reside in the oceans where they either merge with another subduction zone or migrate in the oceans before reaching a continental margin where they endure for some time before ceasing (Figure 5). In some cases, a subduction zone retreats toward the continent and once it hits the margin, subduction continues with a reversed polarity (Figure 2). Rarely, a subduction zone is formed and ceases as intra-oceanic without colliding with another convergence zone (Figure 5). In the weak lithosphere case, termination is random just like initiation (Figure 3a). Where the continents have an influence, subduction zones are more likely to terminate adjacent to continents than to initiate there, which is presumably a consequence of intra-oceanic subduction zones being able to migrate freely, but once they migrate to a continental margin subduction zones stay there until they cease (Figure 3b and c).

3.2. Influence of number of continental margins

Repeated continental assembly and dispersal are observed on Earth in the cycles that last for several 100 Myr [e.g. Rogers and Santosh, 2004]. The length of the continental margins thus varies according to the continental configuration, being minimal when continents are aggregated and maximal when dispersed. To investigate the influence of the number of continental margins on the position of subduction initiation within our annulus models, we perform a set of calculations with one, two and three continental rafts (where each raft has two margins), while keeping the total cover of continents constant at 30% of the annulus. The number of continental margins in 2D models corresponds to the length of the continental margins in 3D. In these models, we keep the yield stress fixed

($\sigma_0 = 35\,\mathrm{MPa}$) and include a weak crustal layer at the surface. The number of subduction zones fluctuates around four or five (cf. histograms on Figure 6). With increasing number of continental margins, the number of intra-oceanic subduction initiations decreases, regardless of whether a weak crustal layer is present (cf. Figure 4b). In particular, subduction initiation at continental margins increases from 30% for the case with one continent to 67% for three continents (cf. Figure 4b and 6). Two fundamental results are consistent across all model cases: firstly, all cases significantly differ from initiation at random position for the chosen lithospheric strength; secondly, we systematically observe that more subduction zones cease at a continental margin compared to the initiation position (cf. Figure 6). Both these relationships are weakest for the case with a single continent (cf. Figure 6a). The threshold distance below which the effect of continents is negligible and the distribution follows a random distribution of subduction initiation increases with increasing number of continental margins and is around 4000 km, 6000 km and 7000 km for cases with two, four and six continental margins (Figure 6).

3.3. Asymmetric subduction zones

At the surface of the Earth, during a collision of two oceanic plates, one of them subducts into the mantle while the overriding plate stays at the surface. Although numerical models still have limited ability to produce such behavior, strong asymmetry of sinking slabs is observed in our models as is described in the beginning of this section. The simplest model, with a free-slip surface and no weak crustal layer features the least realistic subduction dipping angles and longer periods of vertical descent. In this case, about 45% of subduction inceptions are adjacent to the continental margins (Figure 7a). For more complex models with more realistic slab dip angles due to lubrication and partial decoupling

at the interface between the two colliding plates (models with the weak crustal layer), it is more likely that subduction initiates at the continental margin; close to 60% of detected subduction zones start in the vicinity of the continent (Figure 7b). This is because the lateral density gradient between continental and oceanic lithosphere produces additional compressive stresses that would drive continents to spread below the free-slip boundary, if the viscosity was low enough. Hence compressive stresses focus at the continent ocean boundary [Nikolaeva et al., 2010; Rolf and Tackley, 2011] and favour subduction initiation. In combination with a weak crustal layer having lower yield stress and hence localizing deformation more easily, more subduction zones initiate at the continental margins. For the models with a free, deformable surface that features more realistic slab dips and stress states, the number of initiation events at the continental margins drops to around 30% (Figure 7c). In this case, the free surface allows the continent to hamper continent spreading by generating a topography that can accommodate a fraction of the stresses at the continent ocean boundary and the lateral density difference between the continents and the mantle through isostasy.

3.4. Reconstructions of subduction, initiation, and cessation

The timing and location of past subduction can be reconstructed from geological and geophysical constraints, though such reconstructions are subject to large uncertainties over the timescales of supercontinent cycles (several hundred Myr). In particular, the lengths and locations of plate boundaries within the oceanic realm far from continents are poorly known, increasingly so further back in time, since the crust that comprised these regions is scarcely preserved at the present day. We compare two reconstructions of subduction history (Figure 8) that are derived by different methods, and use these as

points of comparison with numerical model behaviour. The first reconstruction maps the extent of subduction zones within a globally self-consistent framework of plate boundary configurations and plate kinematics [Müller et al., 2016]; the second reconstruction uses subducted slab signatures mapped within seismic tomography models as the primary line of evidence [van der Meer et al., 2010, 2012]. Both reconstructions attempt to reconcile geologic observations from arc remnants to some extent, but nonetheless differ in many aspects - notably, slab remnants interpreted from seismic tomography suggest a much larger population of intra-oceanic subduction zones. Qualitatively, subduction zones in the Müller et al. [2016] reconstruction are typically closer to the continents compared to those in the interpretation of van der Meer et al. [2010, 2012] (Figure 8). Below we describe a first-order quantification of the proximity to continents of subducting segments and their initiation and cessationin both reconstructions, which offers some degree of comparison with the results of the numerical simulations described in Section 2.2. The supporting material contains the computer code and data files used to perform this analysis and a detailed explanation of the steps we followed.

In computing distributions functions for reconstructions, uncertainty arises when we attempt to measure the distance from individual segments along a subduction zone to the nearest continent - such measurements require a clear definition of what does and does not constitute a continent within the reconstructions. The distinction is not clear-cut for the Earth, which contains a spectrum of stretched, submerged continental fragments that have not conventionally been considered continents [e.g. Mortimer et al., 2017], and where the nature of the crust in the overriding plate can change significantly along strike for individual arcs (for example the present-day Aleutian arc). Using a set of reconstructable

polygons defining major continental blocks (Figure 8, see also supporting information) we first derived the curves in Figure 9 by generating sets of randomly distributed points within the oceans at different reconstruction times. We then compute the distance of each point to the nearest continent boundary, and plot the cumulative distribution functions of these distances subdivided into 25 Myr time windows. These results provide a visual baseline to show how the distances to the continents of subduction segments compare to the pattern expected from a random process, similar to that used in Figures 3, 6 and 7 but on a spherical Earth rather than an annulus.

For the Müller et al. [2016] reconstruction, we extract subduction zone geometries at 1 Myr intervals and resample each line geometry to uniformly spaced half-degree segments. We compute the distance of segment mid-points to the nearest continent boundary, such that the distances that contribute to the cumulative distributions may vary significantly along each distinct line feature. These distances are illustrated for each reconstruction time in animation S2, and form the basis of the cumulative distribution functions in Figure 9b where the results are subdivided into 25 Myr time bins. Subduction initiation and termination is not explicitly encoded into the kinematic reconstruction, and so we used simple criteria to detect initiating and ceasing segments. The main criterion is that initiating or ceasing segments will not lie within a threshold distance of any segment from the network of subduction zones from 1 Myr earlier or later. The threshold is required because trenches where subduction is ongoing will migrate by a finite amount over 1 Myr (animation S2), and we use a threshold distance of 200 km to allow for the magnitude of trench migration expected within 1 Myr [Williams et al., 2015]. An exception to this criterion is segments that lie within this threshold distance, but where the pair of plates

that bound the adjacent segments differs between successive plate boundary snapshots 1 Myr apart (occurring for example in cases of reconstructed subduction polarity reversal, which we consider as termination of existing subduction and initiation of a new segment). Locations of subduction initiation and cessation defined in this way are highlighted in animation S2, and the distances to the nearest continents at these points form the basis of the cumulative distribution functions in Figure 9c.

For subduction history interpreted from seismic tomography, we compute the distance to the nearest continent of the line geometries defined by these previous studies at discrete reconstruction times being 7 to 17 Myr apart. We make an important distinction between slabs tabulated in van der Meer et al. [2010] (Figure 9e) and the longer list of slabs considered in van der Meer et al. [2012] (Figure 9d). For the former, the top and bottom slab ages are available and we take them as the timings of subduction termination and initiation respectively. The histories of additional slabs mapped in van der Meer et al. [2012] are not defined with the same level of detail. Consequently we do not include pre-Cenozoic subduction interpreted from slab remnants beneath the Pacific in two of our distribution plots (Figure 9e,f).

With these limitations in mind, we ask the question as to whether the patterns of subduction initiation and cessation contained within current reconstructions follow a similar distribution to that observed in our numerical models. The distribution of subduction in relation to continents from the alternative subduction histories is illustrated using cumulative distribution functions (Figure 9), providing some analogy to the annulus model results. For both subduction histories, the overall distribution of ongoing subduction is typically closer to the continents than expected for randomly distributed points within

the oceans (Figure 9b,d,e). This pattern is particularly pronounced for the Müller et al. [2016] kinematic reconstruction (Figure 9b), which lacks many intra-oceanic systems interpreted by van der Meer et al. [2010, 2012] from seismic tomography. When we isolate subduction initiation and cessation (Figure 9c,f), a further trend emerges that is apparent in both kinematic and tomography-based subduction histories - subduction cessation is typically closer to the continents than subduction initiation. This trend is only absent in the poorly resolved pre-100 Ma section of the Müller et al. [2016] reconstruction and the results do not show an obvious distinction between the periods before and after 100 Ma, broadly corresponding to the periods of initial and later stages of dispersal of Pangea. However, since the distributions for tomography-based initiation and termination do not include additional slabs interpreted to have existed within the middle of the Panthalassic ocean (Figure 8), the proportion of cases far from continents while Pangea was assembled are likely to be underestimated in our plots.

4. Discussion

Previous studies into the effect of continents on mantle dynamics have shown that continents increase the wavelength of the convective flow [e.g. Guillou and Jaupart, 1995] and influence heat loss out of the system as they act as thermal insulators [e.g. Lenardic and Moresi, 1999; Rolf et al., 2012]. Importantly, numerical simulations and laboratory experiments suggest that continents change the lithospheric stress distribution and facilitate subduction initiation [e.g. Nikolaeva et al., 2010; Rolf and Tackley, 2011]. However, systematic study of the locations of subduction initiation and their ensuing evolution taking into account global tectonic settings has received very little attention.

Comparison between the distribution of subduction in numerical simulations and those inferred from reconstructions offers insight into the most plausible model parameters. Models in which the lithospheric strength is low, such that subduction is effectively randomly distributed within the oceans, are inconsistent with the inferred patterns of subduction on Earth during the last >200 Myr (Figure 9). Instead, the distributions from reconstructions are more compatible with scenarios in which the lithospheric strength is relatively high, such that the continents generate a strain shadow promoting subduction initiation closer to the continents. This region adjacent to margins is loaded by the density and topography contrast between continent and ocean lithosphere. Therefore, the lithosphere more readily yields upon experiencing additional stresses produced by convection, whereas the same convective stresses alone are less likely to reach the yield criterion further from continents.

In models where sites of initiation of subduction are biased towards regions close to continents, the distribution of subduction throughout its duration and cessation is also naturally biased towards these regions. Subduction that initiates at a continental margin remains there until it ceases. Subduction systems initiating in the oceans may migrate towards or away from the nearby continental margins; those that reach the continent margin become continental arcs, and remain so until subduction ceases. Hence, the control of continents on patterns of subduction initiation influences the distribution of subduction cessation, such that subduction termination along continental margins occurs more frequently than subduction initiation, even in the absence of continent-continent collision.

Comparison between models with different numbers of continents (and therefore margins) offers an insight into the different distributions of subduction that we may expect

during different phases of the supercontinent cycle. Cases with two or three distinct continents (analogous to periods of continental dispersal such as the last ∼100 Myr on Earth) are more favorable to subduction initiation close to continental margins - in contrast, when the annulus includes only one continent (analogous to a supercontinent such as Pangea), the area influenced by the continental strain shadow effect is reduced and the proportion of subduction initiations (and terminations) occurring within the oceans increases. This result contrasts with the results for the Müller et al. [2016] kinematic reconstruction, where very little subduction initiates, evolves, or ceases far from continents prior to 100 Ma (Figure 9b,c). However, distributions from kinematic reconstructions also contrast with those for alternative subduction histories interpreted from seismic tomography - in particular when these take into account Triassic-Jurassic, intra-Panthalassa subduction systems of van der Meer et al. [2012], illustrated in Figure 8 and included in the distribution of Figure 9d but not included in Figure 9f. The ages and locations of subduction initiation for these systems is unknown, but it is reasonable to infer that some or all of these systems initiated far from Pangea.

In addition to the global studies of van der Meer et al. [2010] and van der Meer et al. [2012], regional studies have also interpreted tomography to reveal previously unrecognised intra-oceanic subduction zones existing within Panthalassa during the Cretaceous and earlier [Domeier et al., 2017; Sigloch and Mihalynuk, 2013]. Furthermore, numerical models of past mantle flow constrained by subduction histories similar to that of Müller et al. [2016] produce present-day temperature fields that show good agreement with deep mantle seismic velocity variations imaged by tomography to first-order [Flament et al., 2017] but yield regional mismatches around parts of the Pacific which may be resolved

when additional intra-oceanic subduction zones are incorporated [e.g. Braz et al., 2018]. The emerging view from observations is that intra-oceanic subduction was more prevalent during Pangea's existence and early breakup than previously recognised. Our model results in which intra-oceanic subduction initiation and evolution is favoured during supercontinental assembly are consistent with this view, even though our models lack many features of real-world plate tectonics. Even during supercontinent assembly we would still expect a greater likelihood of intra-oceanic subduction initiation proximal to continental margins in the geological record [e.g. Maffione et al., 2017].

One must keep in mind that numerical simulations have certain limitations. Primarily, the study relies on 2D calculations, in which only poloidal flow can exist. We do not consider any 3D characteristics of mantle flow such as toroidal motion around lateral slab edges that can slow down descending slabs [Li and Ribe, 2012]. The models operate at a Rayleigh number that is lower than the Earth's and hence result in thicker boundary layers, less vigorous convection and surface heat flow and plate velocities lower than what is expected for our planet. Although basal heating in the models (representing around 20% of the total surface heat flux) falls into the estimated range of the Earth's basal heat flux portion [Jaupart et al., 2015], we fix the internal heating rate and we possibly underestimate the influence of plumes. Subduction can be initiated when plumes provide sufficient additional stresses causing local weakening of the lithosphere after hitting the subsurface [Gerya et al., 2008]. However, this is not our case since the plumes in the models are relatively weak and hence only rarely trigger the formation of new convergent boundaries. Importantly, the employed rheology neglects any past deformation of the lithosphere and reflects only the instantaneous stress distribution. However, on Earth

plates have memory of previous yielding and can be damaged or undergo healing [e.g Bercovici and Ricard, 2016].

5. Conclusions

We present an assessment of where subduction initiates and ceases in global convection models with a plate-like surface and continental drift. We compare the results of numerical simulations with distributions of subduction initiation and cessation retrieved from plate tectonics reconstructions and seismic tomography models. We show that the location of subduction initiation and cessation is not randomly distributed within the oceans on Earth. Subduction zones that are formed at continental margins tend to stay there, while subduction zones formed within the oceans migrate and merge with other intra-oceanic subduction zones, or reach continental margins where subduction usually continues, changing polarity before eventually ceasing. Hence, we systematically find that more subduction zones cease in the vicinity of continental margins compared to subduction initiation. Numerical models indicate that the critical parameters that influence the position of subduction initiation are the lithospheric strength and the number of continental margins. Stronger lithosphere (which implies larger plates and fewer subduction zones [Tackley, 2000b]) increases the probability of subduction initiation in the vicinity of continental margins. With our numerical simulations we also predict that intra-oceanic subduction initiation is more likely during the times of supercontinent assembly, while continental dispersal favors incipient subduction close to continents. These results favour interpretations of intra-oceanic subduction systems within the Panthalassa Ocean during the time of Pangea based on seismic tomography [van der Meer et al., 2012; Van Der Meer et al., 2014], which are missing from earlier plate tectonic reconstructions.

Acknowledgments. The support for this research has been provided by the European Union's Horizon 2020 research and innovation program under the ERC grant agreement n°617588 and the Marie Skłodowska Curie grant agreement n°753755. Simulations were performed on the AUGURY super-computer at P2CHPD Lyon. The StagPy library was used in this study to process StagYY output data (`https://github.com/StagPython/StagPy`). The pygplates library was used to analyse plate tectonic reconstructions (`https://www.gplates.org/docs/pygplates/`).

References

Auzende, J.M., Lafoy, Y., Marsset, B., 1988. Recent geodynamic evolution of the north Fiji basin (southwest Pacific). Geology 16, 925–929.

Baes, M., Sobolev, S.V., Quinteros, J., 2018. Subduction initiation in mid-ocean induced by mantle suction flow. Geophys. J. Int. 215, 1515–1522.

Bercovici, D., Ricard, Y., 2016. Grain-damage hysteresis and plate tectonic states. Phys. Earth Planet. Inter. 253, 31 – 47.

Braz, C., Seton, M., Flament, N., Müller, R.D., 2018. Geodynamic reconstruction of an accreted cretaceous back-arc basin in the northern andes. Journal of Geodynamics 121, 115–132.

Christensen, U.R., 1985. Heat transport by variable viscosity convection ii: pressure influence, non-newtonian rheology and decaying heat sources. Physics of the Earth and Planetary Interiors 37, 183 – 205.

Coltice, N., Gérault, M., Ulvrová, M., 2017. A mantle convection perspective on global tectonics. Earth-Sci. Rev. 165, 120 – 150.

562 Coltice, N., Rolf, T., Tackley, P.J., Labrosse, S., 2012. Dynamic causes of the relation
563 between area and age of the ocean floor. Science 336, 335–338.
564 Crameri, F., Schmeling, H., Golabek, G.J., Duretz, T., Orendt, R., Buiter, S.J.H., May,
565 D.A., Kaus, B.J.P., Gerya, T.V., Tackley, P.J., 2012. A comparison of numerical sur-
566 face topography calculations in geodynamic modelling: an evaluation of the sticky air
567 method. Geophys. J. Int. 189, 38–54.
568 Crameri, F., Tackley, P.J., 2014. Spontaneous development of arcuate single-sided sub-
569 duction in global 3-D mantle convection models with a free surface. J. Geophys. Res.:
570 Solid Earth 119, 5921–5942.
571 Dilek, Y., Furnes, H., 2009. Structure and geochemistry of tethyan ophiolites and their
572 petrogenesis in subduction rollback systems. Lithos 113, 1–20.
573 Doin, M.P., Fleitout, L., Christensen, U., 1997. Mantle convection and stability of depleted
574 and undepleted continental lithosphere. J. Geophys. Res.: Solid Earth 102, 2771–2787.
575 Domeier, M., Shephard, G.E., Jakob, J., Gaina, C., Doubrovine, P.V., Torsvik, T.H.,
576 2017. Intraoceanic subduction spanned the Pacific in the Late Cretaceous–Paleocene.
577 Science Advances 3, eaao2303.
578 Flament, N., Williams, S., Müller, R., Gurnis, M., Bower, D.J., 2017. Origin and evolution
579 of the deep thermochemical structure beneath eurasia. Nature communications 8, 14164.
580 Gerya, T., Stern, R., Baes, M., Sobolev, S., Whattam, S., 2015. Plate tectonics on the
581 earth triggered by plume-induced subduction initiation. Nature 527, 221–225.
582 Gerya, T.V., Connolly, J.A., Yuen, D.A., 2008. Why is terrestrial subduction one-sided?
583 Geology 36, 43–46.

584 Guillou, L., Jaupart, C., 1995. On the effect of continents on mantle convection. J.
585 Geophys. Res.: Solid Earth 100, 24217–24238.
586 Hegarty, K.A., Weissel, J.K., Hayes, D.E., 1982. Convergence at the Caroline-Pacific Plate
587 Boundary: Collision and Subduction. American Geophysical Union. pp. 326–348.
588 Hernlund, J.W., Tackley, P.J., 2008. Modeling mantle convection in the spherical annulus.
589 Phys. Earth Planet. Inter. 171, 48–54.
590 Jaupart, C., Labrosse, S., Lucazeau, F., Mareschal, J., 2015. 7.06 - temperatures, heat
591 and energy in the mantle of the earth, in: Schubert, G. (Ed.), Treatise on Geophysics
592 (Second Edition). Elsevier, Oxford. volume 7, Second edition edition. pp. 223–270.
593 Kerrick, D.M., 2001. Present and past nonanthropogenic co2 degassing from the solid
594 earth. Reviews of Geophysics 39, 565–585.
595 Langemeyer, S.M., Lowman, J.P., Tackley, P.J., 2018. The sensitivity of core heat flux to
596 the modeling of plate-like surface motion. Geochem., Geophys., Geosyst. 19, 1282–1308.
597 Lebrun, J.F., Lamarche, G., Collot, J.Y., 2003. Subduction initiation at a strike-slip
598 plate boundary: The cenozoic pacific-australian plate boundary, south of new zealand.
599 Journal of Geophysical Research: Solid Earth 108.
600 Lee, S.M., 2004. Deformation from the convergence of oceanic lithosphere into Yap trench
601 and its implications for early-stage subduction. J. Geodynamics 37, 83 – 102.
602 Lenardic, A., Moresi, L.N., 1999. Some thoughts on the stability of cratonic lithosphere:
603 Effects of buoyancy and viscosity. J. Geophys. Res.: Solid Earth 104, 12.
604 Leng, W., Gurnis, M., 2015. Subduction initiation at relic arcs. Geophys. Res. Lett. 42,
605 7014–7021.

606 Li, Z.H., Ribe, N.M., 2012. Dynamics of free subduction from 3-d boundary element
607 modeling. Journal of Geophysical Research: Solid Earth 117.

608 Lowman, J.P., 2011. Mantle convection models featuring plate tectonic behavior: An
609 overview of methods and progress. Tectonophys. 510, 1–16.

610 Maffione, M., van Hinsbergen, D.J., de Gelder, G.I., van der Goes, F.C., Morris, A.,
611 2017. Kinematics of Late Cretaceous subduction initiation in the neo-tethys ocean
612 reconstructed from ophiolites of Turkey, Cyprus, and Syria. J. Geophys. Res.: Solid
613 Earth 122, 3953–3976.

614 Matsumoto, T., Tomoda, Y., 1983. Numerical simulation of the initiation of subduction
615 at the fracture zone. Journal of Physics of the Earth 31, 183–194.

616 van der Meer, D.G., Spakman, W., Van Hinsbergen, D.J., Amaru, M.L., Torsvik, T.H.,
617 2010. Towards absolute plate motions constrained by lower-mantle slab remnants. Nat.
618 Geosci. 3, 36–40.

619 van der Meer, D.G., Torsvik, T.H., Spakman, W., Van Hinsbergen, D.J.J., Amaru, M.L.,
620 2012. Intra-panthalassa ocean subduction zones revealed by fossil arcs and mantle
621 structure. Nat. Geosci. 5, 215–219.

622 Michaud, F., Royer, J.Y., Bourgois, J., Dyment, J., Calmus, T., Bandy, W., Sosson, M.,
623 Mortera-Gutiérrez, C., Sichler, B., Rebolledo-Viera, M., et al., 2006. Oceanic-ridge
624 subduction vs. slab break off: Plate tectonic evolution along the baja california sur
625 continental margin since 15 ma. Geology 34, 13–16.

626 Moresi, L., Solomatov, V., 1998. Mantle convection with a brittle lithosphere: thoughts
627 on the global tectonic styles of the earth and venus. Geophys. J. Int. 133, 669–682.

628 Mortimer, N., Campbell, H.J., Tulloch, A.J., King, P.R., Stagpoole, V.M., Wood, R.A.,
629 Rattenbury, M.S., Sutherland, R., Adams, C.J., Collot, J., et al., 2017. Zealandia:
630 Earths hidden continent. GSA Today 27, 27–35.

631 Müller, R., Landgrebe, T., 2012. The link between great earthquakes and the subduction
632 of oceanic fracture zones. Solid Earth 3, 447–465.

633 Müller, R.D., Seton, M., Zahirovic, S., Williams, S.E., Matthews, K.J., Wright, N.M.,
634 Shephard, G.E., Maloney, K.T., Barnett-Moore, N., Hosseinpour, M., Bower, D.J.,
635 Cannon, J., 2016. Ocean Basin Evolution and Global-Scale Plate Reorganization Events
636 Since Pangea Breakup. Ann. Rev. Earth Planet. Sci. 44, 107–138.

637 Nikolaeva, K., Gerya, T.V., Marques, F.O., 2010. Subduction initiation at passive mar-
638 gins: Numerical modeling. J. Geophys. Res.: Solid Earth 115, B03406.

639 Reagan, M.K., Ishizuka, O., Stern, R.J., Kelley, K.A., Ohara, Y., Blichert-Toft, J.,
640 Bloomer, S.H., Cash, J., Fryer, P., Hanan, B.B., et al., 2010. Fore-arc basalts and
641 subduction initiation in the izu-bonin-mariana system. Geochem., Geophys., Geosyst.
642 11.

643 Rogers, J., Santosh, M., 2004. Continents and Supercontinents. Oxford University Press.

644 Rolf, T., Coltice, N., Tackley, P., 2012. Linking continental drift, plate tectonics and the
645 thermal state of the Earth's mantle. Earth Planet. Sci. Lett. 351, 134–146.

646 Rolf, T., Tackley, P., 2011. Focussing of stress by continents in 3D spherical mantle
647 convection with self-consistent plate tectonics. Geophys. Res. Lett. 38.

648 Sigloch, K., Mihalynuk, M.G., 2013. Intra-oceanic subduction shaped the assembly of
649 cordilleran north america. Nature 496, 50.

650 Stern, R.J., 2004. Subduction initiation: spontaneous and induced. Earth Planet. Sci.
651 Lett. 226, 275–292.

652 Tackley, P.J., 2000a. The Quest for Self-Consistent Generation of Plate Tectonics in
653 Mantle Convection Models. American Geophysical Union, Washington, D.C.. volume
654 121 of *Geophys. Monograph.* pp. 47–72.

655 Tackley, P.J., 2000b. Self-consistent generation of tectonic plates in time-dependent,
656 three-dimensional mantle convection simulations 1. pseudoplastic yielding. Geochem.,
657 Geophys., Geosyst. 1.

658 Tackley, P.J., 2008. Modelling compressible mantle convection with large viscosity con-
659 trasts in a three-dimensional spherical shell using the yin-yang grid. Phys. Earth Planet.
660 Inter. 171, 7–18.

661 Tackley, P.J., King, S.D., 2003. Testing the tracer ratio method for modeling active
662 compositional fields in mantle convection simulations. Geochem., Geophys., Geosyst.
663 4, 8302.

664 Ulvrova, M.M., Brune, S., Williams, S., 2019. Breakup without borders: How continents
665 speed up and slow down during rifting. Geophysical Research Letters 46, 1338–1347.

666 Van Der Meer, D.G., Zeebe, R.E., van Hinsbergen, D.J., Sluijs, A., Spakman, W., Torsvik,
667 T.H., 2014. Plate tectonic controls on atmospheric co2 levels since the triassic. Proc.
668 Nat. Acad. Sci. 111, 4380–4385.

669 Williams, S., Flament, N., Müller, R.D., Butterworth, N., 2015. Absolute plate motions
670 since 130 ma constrained by subduction zone kinematics. Earth and Planetary Science
671 Letters 418, 66–77.

Variable	*Symbol*	*Nondimensional Value*	*Dimensional Value*
Gravitational acceleration	g	-	$9.81\,\mathrm{m\,s^{-2}}$
Mantle thickness	D	1	$2890\,\mathrm{km}$
Thermal expansivity	α_0	-	$3 \times 10^{-5}\,\mathrm{K^{-1}}$
Thermal diffusivity	κ	-	$10^{-6}\,\mathrm{m^2\,s^{-1}}$
Thermal conductivity	k	-	$4\,\mathrm{W\,m^{-1}\,K^{-1}}$
Gas constant	R	-	$8.314\,\mathrm{J\,mol^{-1}\,K^{-1}}$
Reference density	ρ_0	1	$3300\,\mathrm{kg\,m^{-3}}$
Internal heating rate	H	20	$5.44 \times 10^{-12}\,\mathrm{W\,kg^{-1}}$
Reference viscosity	η_0	1	$6 \times 10^{22}\,\mathrm{Pa\,s}$
Activation energy	E_a	8	$170\,\mathrm{kJ\,mol^{-1}}$
Activation volume	V_a	3	$6.34 \cdot 10^{-7}\,\mathrm{m^3\,mol^{-1}}$
Surface temperature	T_s	0.12	300 K
Superadiabatic temperature drop	ΔT	1	$2500\,\mathrm{K}$
Rayleigh number	Ra	10^6	-
Surface yield stress in oceans	σ_0	10^3 to 8×10^3	7 MPa to 56 MPa
Yield stress depth derivative in oceans	σ'_Y	3.3×10^5	$810\,\mathrm{Pa\,m^{-1}}$

Table 1. Dimensional and non-dimensional parameters of the convection model.

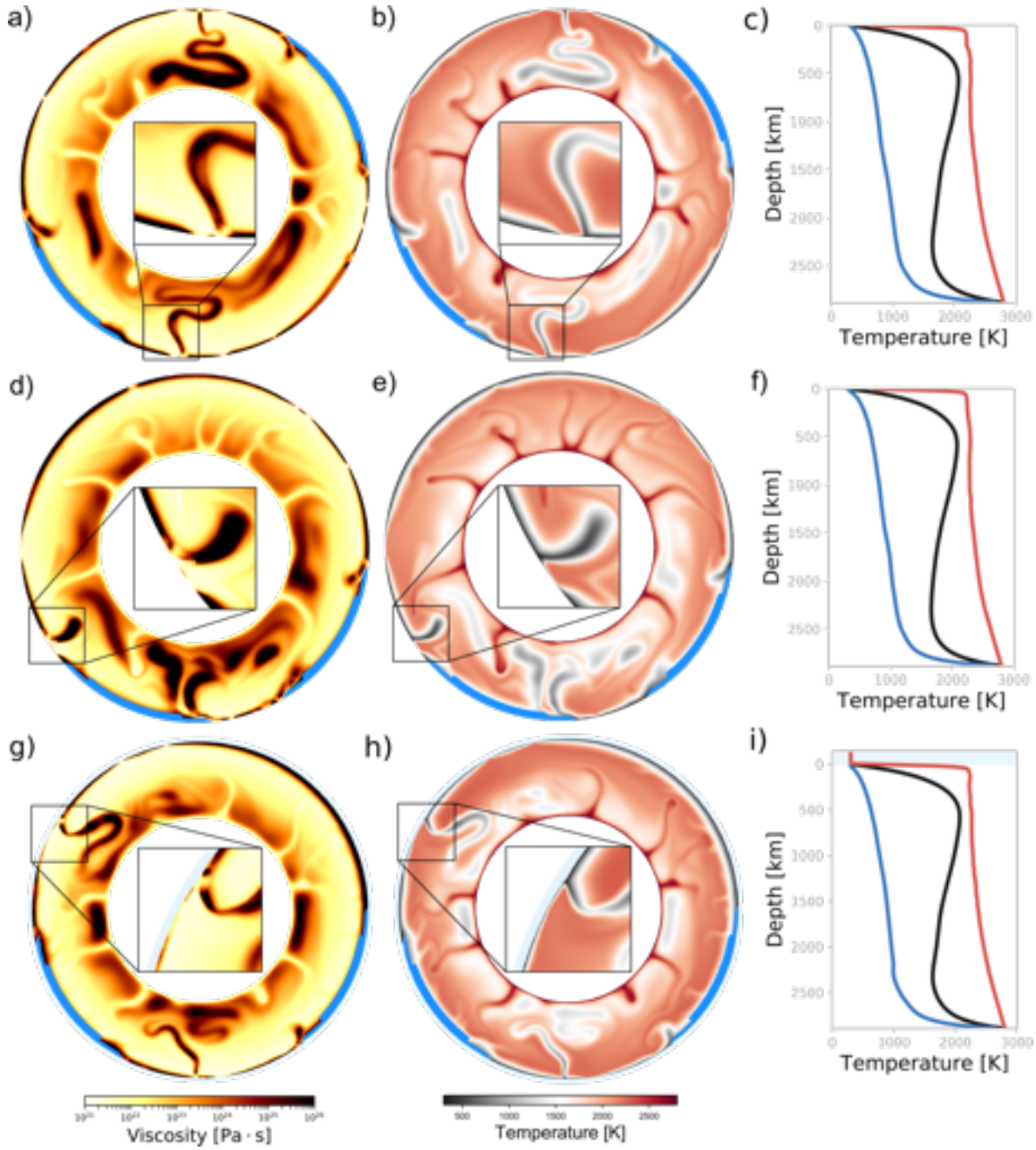

Figure 1. A snapshot of the viscosity (left column) and temperature (middle column) fields at one particular time. (Right column) Azimuthally and temporally averaged temperature profiles of minimum (blue), mean (black) and maximum (red) temperature. Model without a)-c) and with d)-f) weak crustal layer. g)-i) Model with free surface. Air layer atop of the mantle is shown in light blue. Continents are emphasized in all panels in blue.

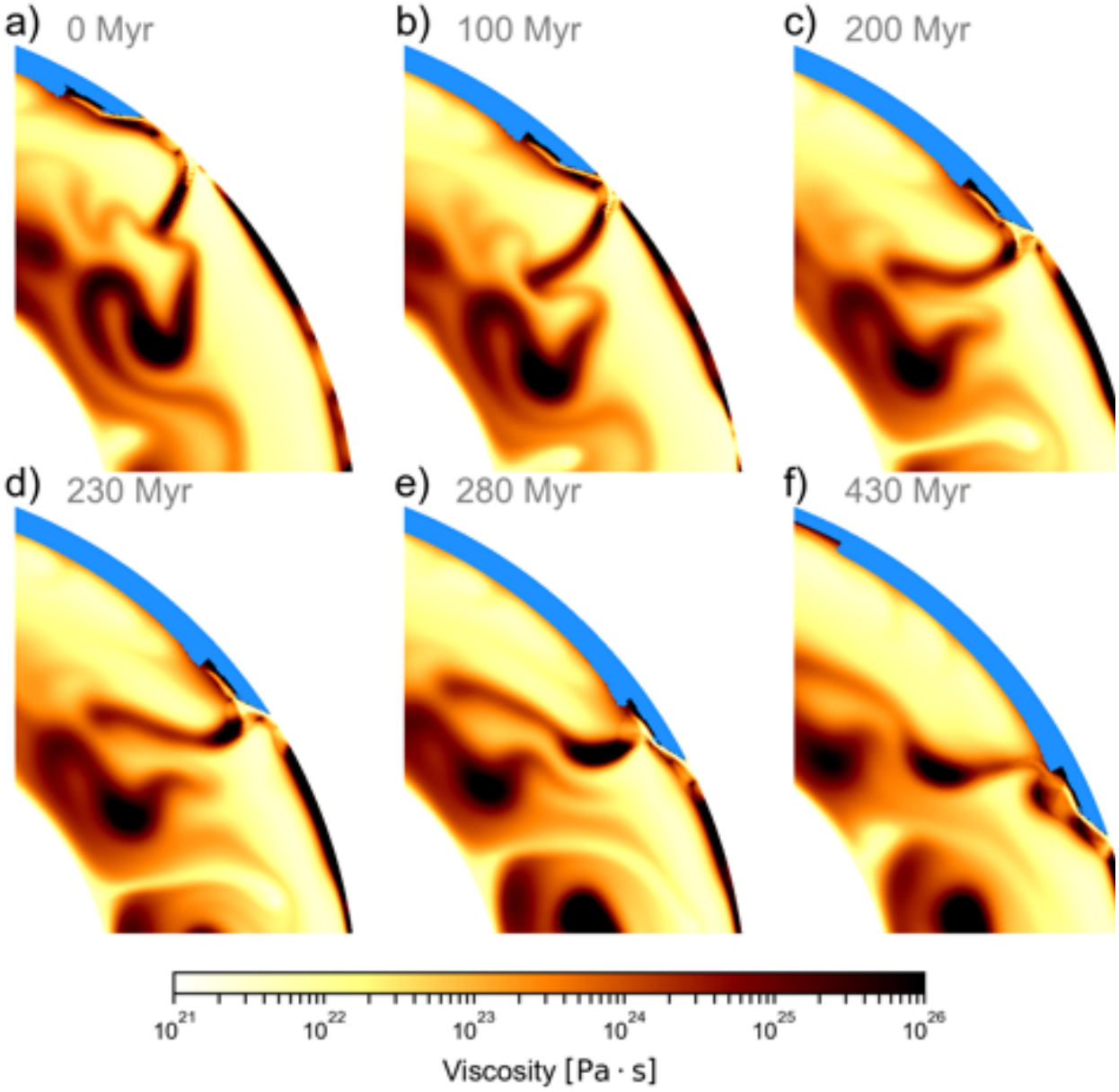

Figure 2. a)-c) Subduction zone retreating toward the continent (emphasized in blue) and reaching the continental margin. d)-f) Subduction zone changes its polarity and continues descending into the mantle next to the margin. The model has a weak crustal layer and intermediate yield stress $\sigma_0 = 35\,\mathrm{MPa}$.

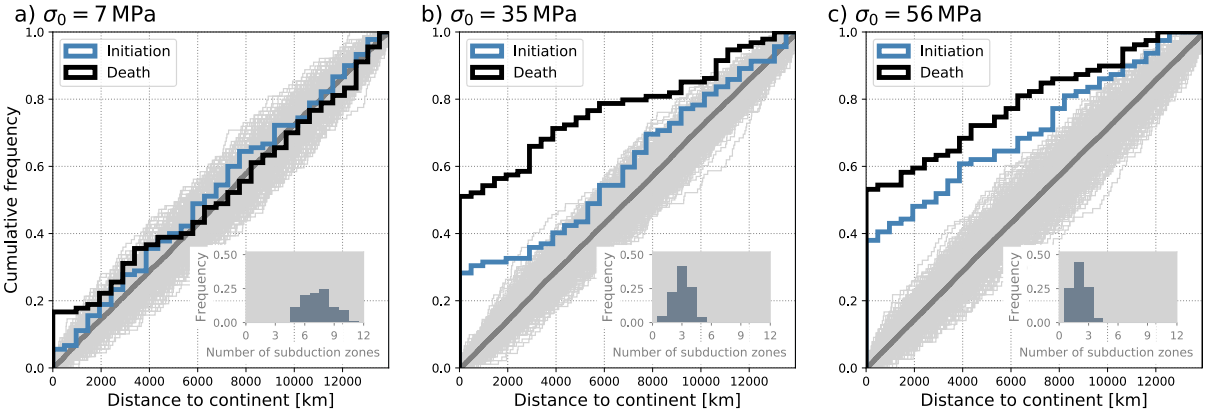

Figure 3. Cumulative distribution of subduction initiation (blue) and cessation (black) as a function of distance from the nearest continent for three different yield stresses σ_0 (increasing from left to right). Dark grey line represents the distribution of subduction initiation at random position for a large population of cases. Gray area designates random distributions generated for N subduction initiations with N being the number of initiations detected for a particular model. Number of subduction zones detected is (from left to right) 89, 93 and 78. Histograms in the bottom right corners show the distribution of the number of subduction zones in the respective models. The models have a free slip top boundary but no weak crustal layer.

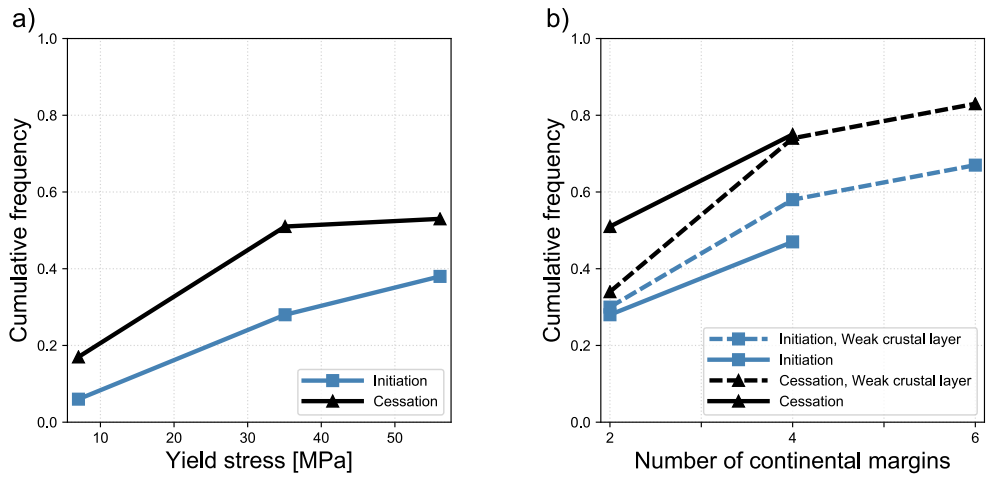

Figure 4. a) Proportion of all subduction zones that initiate (blue) and cease (black) in the vicinity of the continent as a function of the lithospheric strength. One continental raft is present (i.e., two margins) throughout the simulations. b) Proportion of all subduction zones that initiate (blue) and cease (black) in the vicinity of the continent as a function of the number of the continental margins. Solid line is for models with compositionally uniform oceanic lithosphere while dashed line is for runs with weak crustal layer. The yield stress is fixed at $\sigma_0 = 35\,\mathrm{MPa}$.

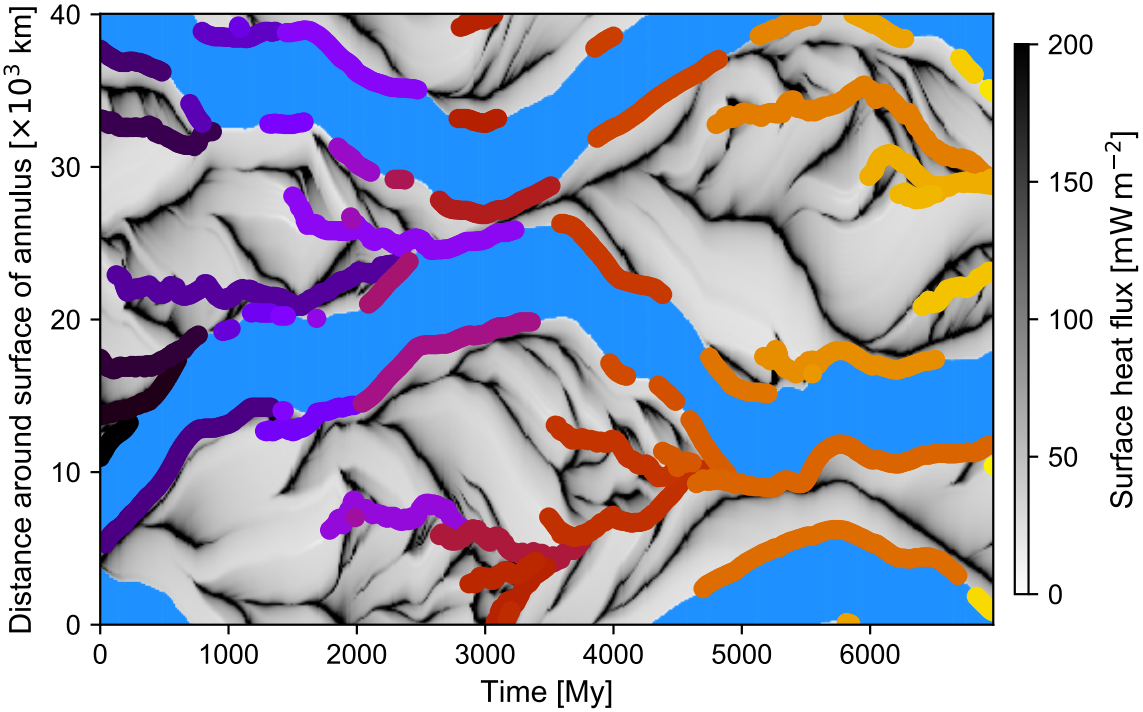

Figure 5. Position of the continents (blue) and subduction zones (coloured lines; one colour corresponds to individual subduction zone) through time together with the surface heat flux (gray scale). The model has a weak crustal layer and intermediate yield stress $\sigma_0 = 35\,\mathrm{MPa}$.

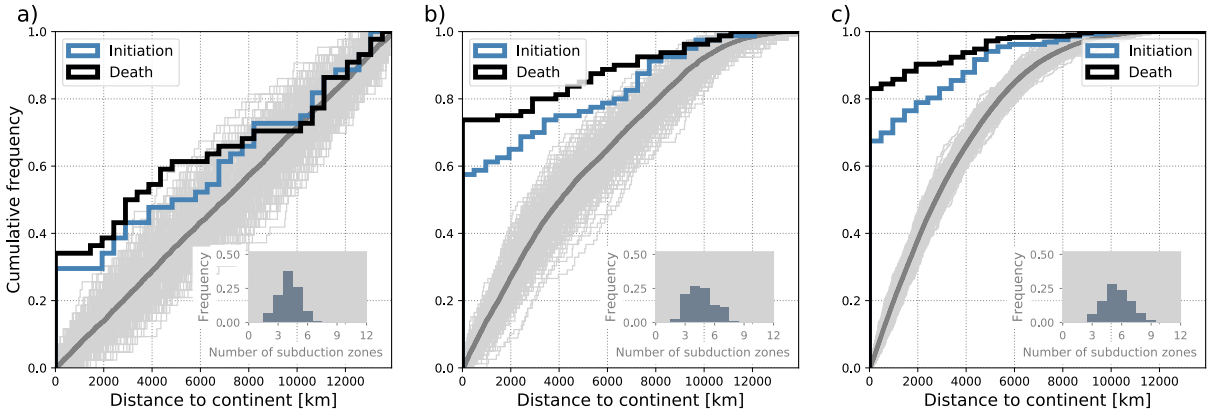

Figure 6. The influence of the number of continental margins (increasing from left to right). a) Two continental margins ($N = 43$), b) four continental margins ($N = 79$), c) six continental margins ($N = 288$). N is the number of initiations detected for a particular model. Dark grey line represents the distribution of subduction initiation at random position for a large population of cases. Gray area designates random distributions generated for N subduction initiations. Histograms in the bottom right corners show the distribution of the number of subduction zones in the respective models. The yield stress is $\sigma_0 = 35\,\mathrm{MPa}$ and the models feature a weak crustal layer.

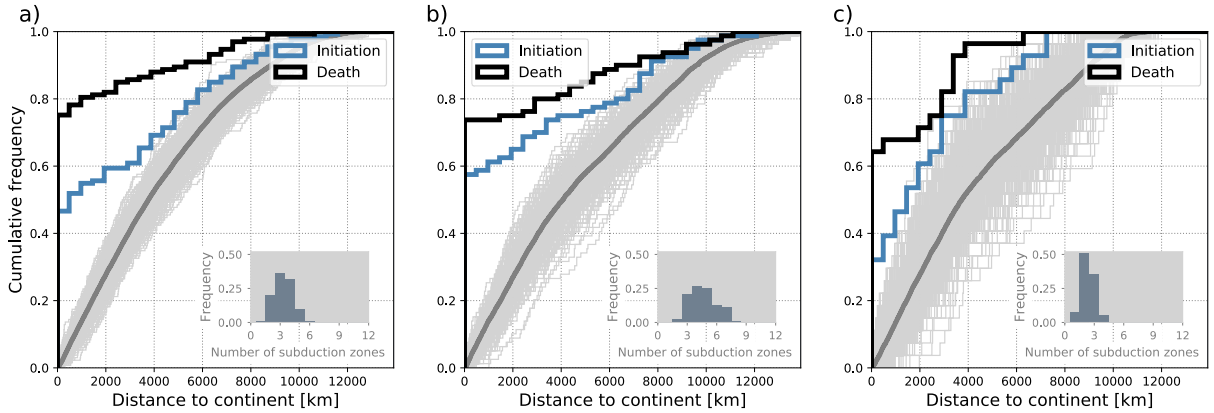

Figure 7. Cumulative distribution of subduction initiation (blue) and cessation (black) for model with a) no weak crustal layer ($N = 132$), b) weak crustal layer ($N = 79$), and c) free surface ($N = 27$). N is the number of subduction initiations detected for a particular model. Dark grey line represents the distribution of subduction initiation at random position for a large population of cases. Gray area designates random distributions generated for N subduction initiations. Histograms in the bottom right corners show the distribution of the number of subduction zones in the respective models. The yield stress is fixed at $\sigma_0 = 35\,\mathrm{MPa}$. There are two continents throughout the simulations.

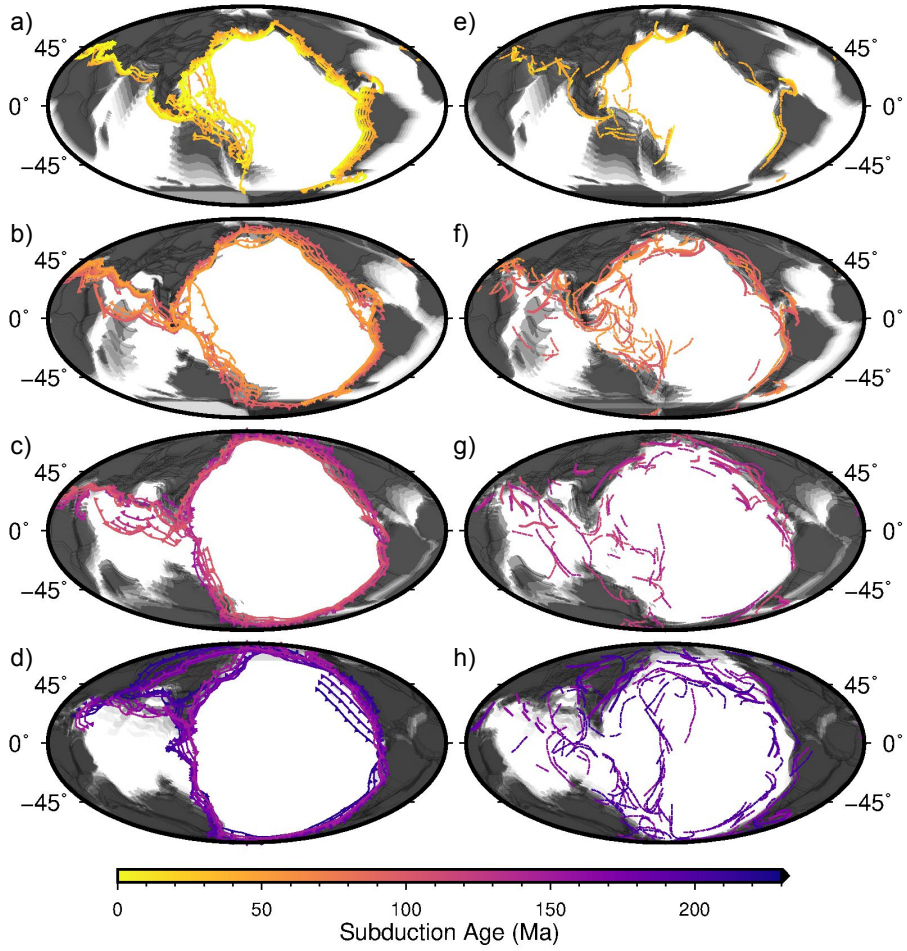

Figure 8. Position of the continents and subduction zones since the Triassic according to two alternative reconstructions (see text), subdivided into 4 distinct time windows from Pangea times to recent. The detailed time-evolution of these reconstructions is illustrated in animations S2-S3. a) Subduction zones and continent positions for the M2016 model between 0 and 50 Ma, plotted at 10 Myr increments; locations of subduction zones are shown in colours corresponding to the color legend, while the continents are shown in gray with darker gray standing for younger positions within the 0-50 Myr period.b) same as a for 50-100 Ma; c) same as a for 100-150 Ma; d) same as a for 150-230 Ma; e) V2012 model for times between 0-50 Ma f) same as e for 50-100 Ma; g) same as e for 100-150 Ma h) same as e for 150-235 Ma.

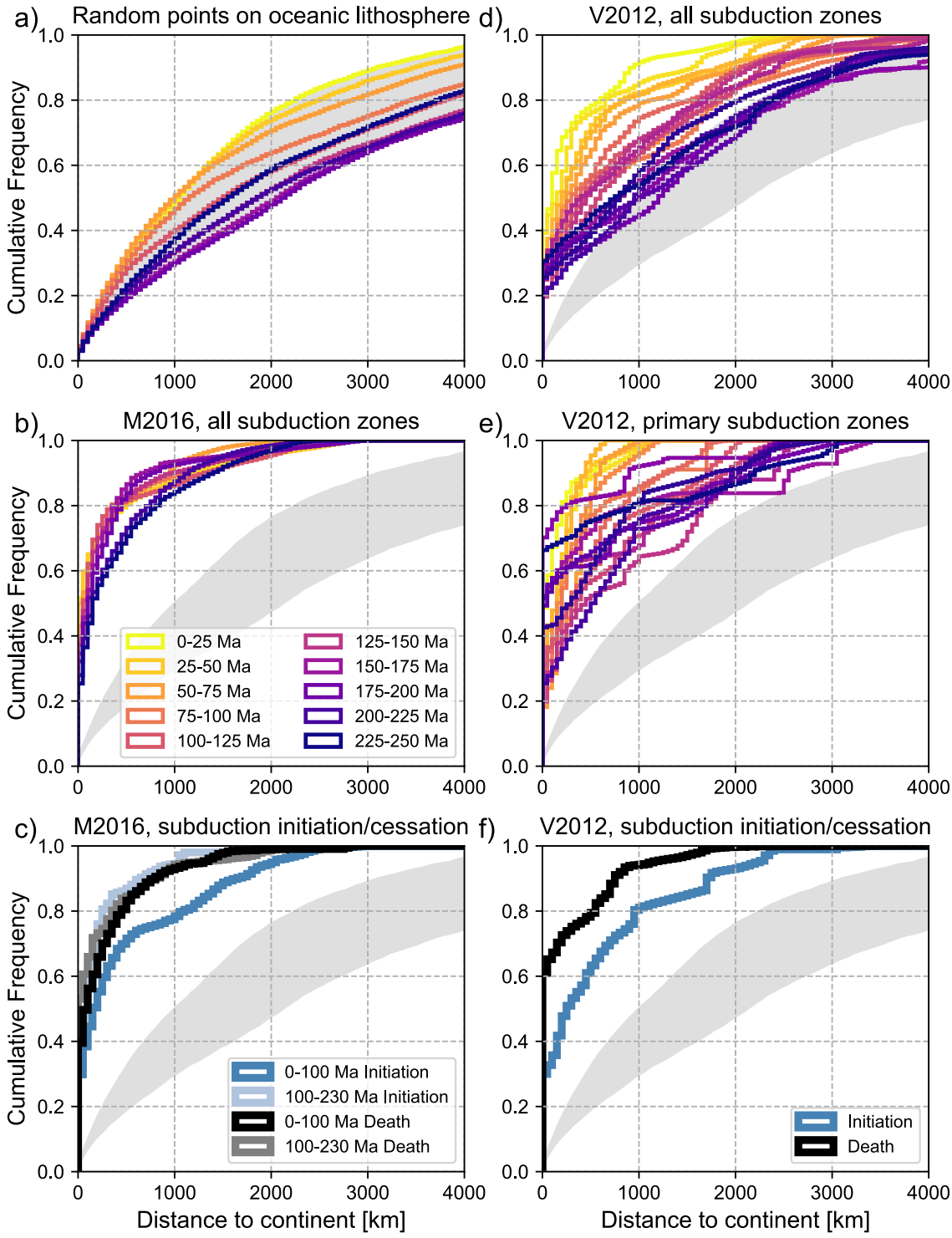

Figure 9. Caption on the next page

Figure 9. Cumulative distribution functions for distance between continents and points along subduction zones at different stages of their development for reconstructions from the Triassic to present (see supporting text and animations S2-S3). Each coloured line represents the distribution for a specific time in panels a, b, d and e. In panels c and f, the relatively small number of initiating and ceasing subduction segments are subdivided into broad time ranges encompassing the earlier and later stages of Pangea breakup. See text for further explanation. (a) CDF for random points falling within reconstructed extent of ocean basins; the grey background shows the envelope of these distributions based on random points, and is reproduced on the other panels for visual reference; (b) distance to continent for segments of active subduction zones for the kinematic reconstruction of Müller et al. [2016]; (c) distances to continent for initiating and ceasing subduction segments derived from Müller et al. [2016]; (d) distance to continent for remnants of past subduction mapped from seismic tomography [van der Meer et al., 2010, 2012]; (e) As (d), but only including 'primary' subduction according to the definition of van der Meer et al. [2010]; (f) distance to continents for subduction zones in (e) at the beginning and end of their lifespans (assumed to approximate initiation and cessation) for the slab remnant reconstruction.